

International Journal of Green Energy



ISSN: (Print) (Online) Journal homepage: https://www.tandfonline.com/loi/ljge20

Structural and Aerodynamic Characteristics Analysis of a Small V-shaped Vertical Axis Wind Turbine Rotor

Mosfequr Rahman, Odari Whyte, Marcel Ilie, Valentin Soloiu & Gustavo Molina

To cite this article: Mosfequr Rahman, Odari Whyte, Marcel Ilie, Valentin Soloiu & Gustavo Molina (2021): Structural and Aerodynamic Characteristics Analysis of a Small V-shaped Vertical Axis Wind Turbine Rotor, International Journal of Green Energy, DOI: <u>10.1080/15435075.2021.1946809</u>

To link to this article: https://doi.org/10.1080/15435075.2021.1946809

	Published online: 05 Jul 2021.
	Submit your article to this journal 🗷
Q ^L	View related articles 🗷
CrossMark	View Crossmark data 🗗





Structural and Aerodynamic Characteristics Analysis of a Small V-shaped Vertical Axis Wind Turbine Rotor

Mosfegur Rahman, Odari Whyte, Marcel Ilie, Valentin Soloiu, and Gustavo Molina

Department of Mechanical Engineering; Georgia Southern University, Statesboro, GA USA

ABSTRACT

A detailed comprehensive study of a proposed V-shaped turbine rotor is performed in order to examine its structural and aerodynamic characteristics. The structural analysis section of this work determined the most structurally sound blade geometry from 3 different blade geometries. Using the chosen blade profile, 8 rotor models are developed and are tested numerically. These rotor models are of different configurations, focusing on an inclination angle of 45 and 60 degrees, blade twist angle of 0 and 5 degrees and number of blades. Four rotor models are taken from the initial tests for further study, 3B45D which is a three-bladed rotor with a 45 degree inclination angle, 5B45D which is a five-bladed rotor with a 45 degree inclination angle and a 5 degree blade twist angle, and 5B60D which is a five-bladed rotor with a 60 degree inclination angle. From the structural study, blade design 2 held the best structural characteristics. The design showed an excellent Von-Mises at 8.8 MPa for static structural and 22.2 MPa for fatigue stress response which is well below the yield strength of ABS Plastic. Both experimental and numerical data have relatively good agreement that is within 15% difference. Overall, maximum power coefficient achieved in this study is about 0.259 numerically and 0.213 experimentally. The best performance is seen by the 3B45D rotor in both static and dynamic study considering experimental and numerical corroboration of results.

ARTICLE HISTORY

Received 28 December 2020 Accepted 9 June 2021

KEYWORDS

Wind energy; vertical axis wind turbine; vawt; v-shaped; structural design; rotor design; renewable energy; clean electricity; cfd

1. Introduction

Globally, the demand for energy is ever-increasing while the dependable sources for the last few centuries become scarcer and the environmental problems they cause loom ever larger. In seeking new renewable and/or carbon-free alternative energy sources, lots of challenges arise in human health risks, cost and economics, political as well as social education about alternatives. Solar and wind energy have proven to be the most common and attractive alternative energy producing mediums available. Of them, wind energy is an inexhaustible resource and helps to reduce the cost of adding renewables to most energy portfolios.

Modern wind turbines are increasingly cost-effective and more reliable, and have scaled up in size to multi-megawatt power ratings. The improvement of power generating capacity by wind turbines has led to a revitalized interest in the development of Vertical Axis Wind Turbines (VAWTs) specifically for offshore energy extraction. Over the last two decades there has been an increased renewed interest in Vertical Axis Wind Turbines. This turbine configuration though unpopular for large-scale generation has found a niche market in the way of offshore energy harvesting. However, offshore wind has its challenges. The vertical axis wind turbine (VAWT) is regarded as an important device to utilize the renewable offshore wind energy to supplement the existing power systems. The conventional horizontal axis wind turbines (HAWTs) present a great deal of inefficiencies and expense when used in offshore

applications. Particularly in deep water (i.e., over 50 meters), conventional HAWTs have a number of limitations for off-shore operations. The majority of VAWTs are some forms of Savonius (drag-type) or Darrieus (lift-type) configuration, or a combination of the two (Gardiner 2011). The novel shape of the NOVA (Novel Offshore Vertical Axis) project turbine, combines a V-rotor with several blades positioned along the span that are angled to minimize the aerodynamic over-turning moments (Wang et al. 2016).

Aside from the type and orientation of a particular wind turbine, one of the most important components of a wind energy collection system is the rotor and blades assembly method. Structural design and performance analysis of wind turbine blade is an important part of the design theory and application of wind turbines (Kong et al. 2006; Ronold and Cristensen 2001). For HAWT blades, only few full scale blades are physically tested during the design process as a confirmation of general structural integrity due to the high cost of carrying out such experiments. By utilizing computational technology and various design approaches, information from these tests can be taken into account in a much more economical way to speed up the design process and increase structural reliability of blades (Toft and Sorensen 2011). There are several important factors which influence the design of efficient and valuable wind turbine performance, but, the most important of these is the design of the blade. The blade efficiency can be affected by variables such as: length, shape, blade twist, material, pitch, and wind speed. The aerodynamic shape of a wind turbine blade is generally optimized in order to achieve better power performance (Liu, Wang, and Tang 2013; Wang, Tang, and Liu 2012a, 2012b). In terms of the structure, wind turbine blades are generally made of composite materials due to their high strength-to-weight ratio and good fatigue performance. In order to meet design requirements, wind turbine blades commonly have complex structural layout, comprising one or more shear webs and a number of composite plies placed at different ply angles (Bir and Migliore 2004; Wang 2015). The structural performance of a composite blade can be tailored by changing stacking sequence, fiber orientation, stacking location and size of the materials (Wang et al.

A novel VAWT structure with V-shaped blade has been investigated to improve the power outputs at moderate tip speed ratios (Su et al. 2020). The Reynolds-Averaged Navier-Stokes SST k - ω turbulence model was applied on the V-shaped VAWT to investigate the aerodynamic performance of such VAWT. Their results indicated that the maximum enhancement in power coefficient obtained in the optimal V-shaped blade was about 24.1%. It was also found that the V-shaped blade could effectively suppress the flow separation and delay the dynamic stall in the middle of the blade, and the undesirable blade tip effect would not be more serious compared to that of the conventional straight blade.

The offshore floating vertical axis wind turbines (OFVAWTs) faced pitch and surge motions of platforms with wind and wave loads. The wake characteristics of an H-rotor floating vertical axis wind turbine under the platform's pitch and surge motions were investigated using the computational fluid dynamics approach with the improved delayed detached eddy simulation (IDDES) (Lei et al. 2019). The wake characteristics under different pitching amplitudes and periods and different surging amplitudes and periods were investigated (Lei et al. 2019). Results showed that pitch motion can enlarge the peak values of wake deficits and shift the positions of the mainstream of the wake in the vertical direction. Wind tunnel testing of floating offshore wind turbines (FOWTs) using a hybrid/hardware-in-the-loop (HIL) methodology was done that was acquired in the last decade through a very intense activity (Belloli et al. 2020). Numerical codes were used within the scientific community to study FOWTs showed significant uncertainties with respect to the prediction of some phenomena like the rotor wind dynamic interaction or the coupling between the machine controller and the lowfrequency rigid-body motion modes of the platform. Conceptual design of a large-scale floating offshore vertical axis wind turbine using a developed aerodynamic modeling strategy has been investigated (Hand and Cashman 2017). This comprehensive examination of several critical VAWT design parameters was undertaken which included the turbine solidity, blade number, blade aspect ratio and non-prismatic strut design. This study identified that a low solidity turbine ($\sigma = 0.263$) gave the best aerodynamic performance. The historical evolution of the lift-type vertical axis wind turbine, from onshore to offshore floating application has been discussed since its inception in the early 1930s (Hand and Cashman 2020). Many curved-bladed and straight-bladed VAWTs were tested and are reviewed. It was found that the VAWT received

very little engineering development in the 1990s due to dominance of the HAWT in the wind energy market. This review also found that the VAWT has entered a Renaissance period whereby the VAWT adopted for the offshore floating wind turbine industry.

Considering these previous endeavors, there are several avenues available to extend the body of knowledge as it currently stands. Firstly, there have been few efforts made to assess the effects of a conventional HAWT blade design without the addition of sectioned airfoil/hydrofoil sections to the blade, on a V-shaped design. Secondly, a great deal of the existing body of research seems to be more focused on the structural longevity of the system rather than the aerodynamic capabilities, and lastly, knowledge of the effects of inclination angle, as well as the application of more than two blades and their effects on power production are limited.

In this current research, a detailed comprehensive study of a V-shaped vertical axis wind turbine (VAWT) rotor is performed in order to examine its structural and aerodynamic characteristics. The structural portion of this study has determined three different blade configurations where root design, overall blade geometry and structural failure features are analyzed. The most structurally sound blade design is then optimized for experimental and numerical aerodynamic testing purposes. In the aerodynamic portion of this study, the selected blade geometry from the structural analysis is applied to eight different rotor designs and analyzed with numerical simulations. 3D static Computational Fluid Dynamics (CFD) analysis using the ANSYS CFX platform is used to determine the effect of inclination angle, wind speed and blade twist angle on power performance. The four best performing turbine rotors based on numerical study are 3D printed and used for wind tunnel experimentation. Experiments are conducted to find reactional torque and rotations per minute (RPM) from which turbine efficiencies are calculated.

It is hypothesized that the proposed V-shaped vertical axis rotor design will produce equivalent energy as a similar sized conventional straight-bladed or helical Darrieus rotor. Also, this research seeks to improve the methods of aerodynamic analysis of vertical axis wind turbine.

2. Model design and fabrication

SolidWorks is used to design three different blades. These designs follow the basic schematic as shown in Figure 1. This layout is used for the structural analysis of the blade. In a fivebladed turbine, blades are identical, and it is assumed that the moments, forces, mode shapes and fatigue assessed in one blade will be identical in all blades during the turbine's operation. So, only one blade is modeled in this study to analyze and estimate the effects of the wind on the turbines structure. It can be seen from Figure 1 that there are two main parts to the blade anatomy, the shoulder and the arm. The blade arm is approximately 18 inches long from the connection at the shoulder to the blade tip. The shoulder length is 2 inches and the radius and height are 14.73 inches and 12.73 inches respectively. For the purpose of the structural study, all models are mounted at an inclination angle of 45° from horizontal plane.

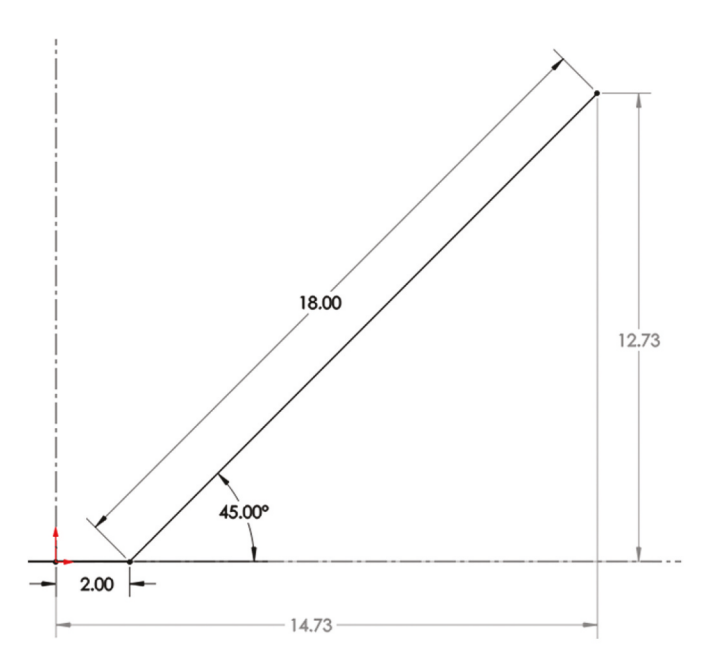


Figure 1. Schematic of intended test blade (dimension in inches).

The three blade designs are illustrated in Figure 2. The specification of each blade design is described in Table 1. The three different blade root connection configurations can be noticed in the table. This is done so that the blade root configuration that is most structurally reliable and easiest to fabricate can be implemented. The central spar type configuration is considered in which foam is chosen as the design material for the ease to affix to the rotor.

2.1. Model development

Selected airfoil shape is applied to produce a working CAD model that is moved to the additive manufacturing stage. The NACA 0015 airfoils are employed to blade design 1 because it is routine to use this design as a starting point for blade profile geometry and it offers the advantage of being easy to work with since blade 1's design is more complex than the other two cases. Blade design 2 is a typical HAWT blade, while design 3 is more akin to a typical Darrieus turbine blade whose geometry is constant throughout the blade profile. Based on the lift and the drag characteristics found from (Xfoil n.d. Xfoil Prediction Polar: NACA 4 Digit Airfoil Generator), the NACA 2414 is chosen to be used for the blade construction of blade design 2 and design 3. NACA 0040 is used in the root of design 2 because it offers good structural characteristics

Table 1. Specifics of three blade designs.

Design	Section	Chord (in)	Profile	Blade Root connection type
1	Shoulder	2.25	NACA0015	Dove-tail
	Arm	1.75	NACA0015	
2	Tip (Arm)	1.00	NACA2414	Male-female socket
	Root	2.50	NACA0040	
3	Tip (Arm)	1.50	NACA2414	Spine insert
	Root			•

having a thicker profile than other profiles mentioned here. The models proposed is exported to an FDM 3D printer and printed by ABS plastic. ABS plastic is made by variation of the ratio of the three monomers Acrylonitrile, Butadiene and Styrene. Because of it high ability to be molded (lending to ease of manufacture), quality surface finish and its ability to flex before rupture, when stress is applied, this plastic is ideal molder for the proposed turbine blades. The 3D printer deposited the ABS plastic layer by layer along with a support material to form the blade structure. The plastic is deposited onto the build surface pad and adheres to it; this allows models to stay in place as the printer head is moving through its path. After the printing is done, the parts can be lifted off using a flat edge, and then is placed in a solution of water and lye to dissolve any remaining support material.

There are two different types of loading when assessing the structural competence of a wind turbine; as illustrated by Figure 3, there is edgewise loading, generated by forces on the blade by the wind and flap wise loading generated by gravity but also by wind in the case of the blade under study.

A cantilever configuration wind turbine blade is applied with the root constrained and the tip free. The gravitational force in the case of the proposed design is in the flapwise direction with wind flow acting in the edgewise direction. Unlike conventional HAWT turbines where gravitational forces affect the blades in the edgewise fashion and the direction of loading is reversed throughout the rotors' travel, many VAWT blades tend not to have this issue as the blades are oriented so that their gravitational forces on the blade are negligible (Barnes, Morozov, and Shankar 2015). Flapwise versus edgewise loading direction is shown in Figure 4.

3. Experimental methods and equipment

An in-house subsonic open-type wind tunnel as shown in Figure 5 is used for the experimental part of this research. Free stream velocity through the test section is easily controlled with the variable frequency drive (VFD) operator interface. The internal fan of the wind tunnel produces wind speeds of

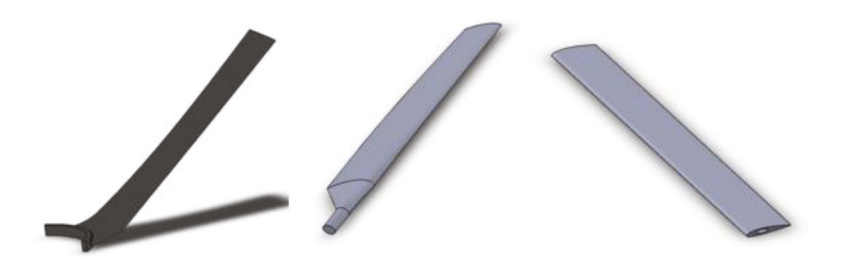


Figure 2. Blade designs 1, 2 and 3 respectively.

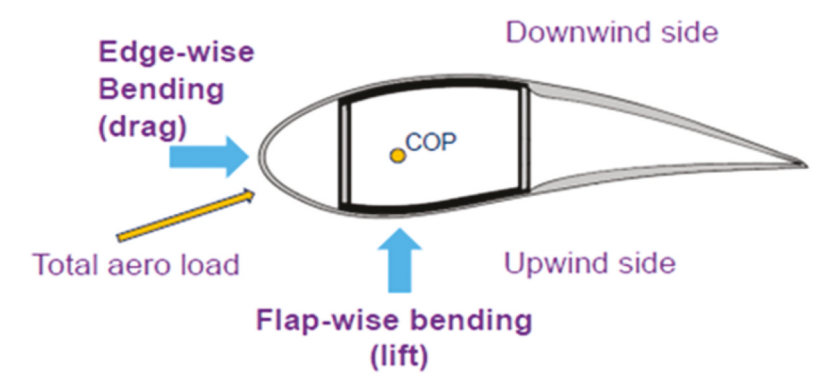


Figure 3. Flap wise vs edgewise loading (Barnes, Morozov, and Shankar 2015).

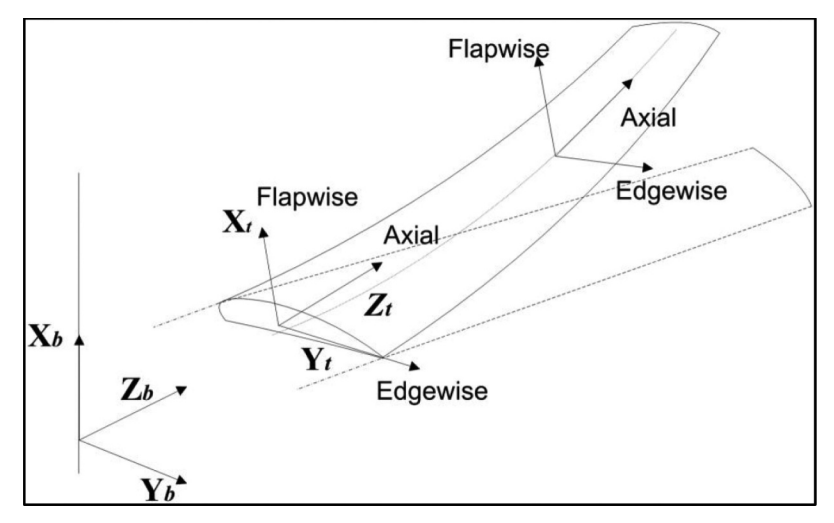


Figure 4. Flapwise vs. edgewisse loading (Barnes, Morozov, and Shankar 2015).



Figure 5. Sub-sonic wind tunnel configuration.

up to 13 m/s through the outlet. A handheld anemometer is used to track wind speeds at the beginning of each run. Anemometer is held about 4–6 inches in front of the model. To ensure consistency and accuracy the measurement is taken over a period of 5 seconds. The La Crosse Technology anemometer has a range of 0.2 m/s to 30 m/s and is accurate to 0.1 m/s, while the CFM Master II is of higher precision, has a measurement range of 0.4 m/s to 35 m/s, and accuracy of $\pm 3\%$.

A reference turbine is the ALEKO* WGV15 Vertical Wind Turbine Generator 15 W – 12 V as shown in Figure 6, a standard 5-bladed H-type Darrieus VAWT, is utilized in order to have a base design.

The hub design allowed for the blades to be adjusted for pitch angle as well as utilize the same hub for multiple rotor configurations. The hub design applied in this work has developed in order to facilitate multiple blade designs to be tested using the same hub and accommodate the variable inclination angle of blades. The RPM of each wind turbine rotor is measured 5 time at each wind speed and then averaged to get the final values. A laser tachometer is used to measure RPM of the models under varying wind conditions. A small piece of reflective tape, indicated by the red arrow in Figure 7, is applied to the top of one blade to reflect the infrared light. A detector on the tachometer receives the reflected light and detects changes in frequency. The frequency change over time gives the rotational speed of the VAWT models. The Omega HHT12 can accurately measure the RPM from angles up to 30 degrees off perpendicular and up to 36 inches from its target. It measures RPMs in the range of 5 to 99,999 RPMs and an accuracy of \pm .01% of reading.



Figure 6. ALEKO WGV15, reference turbine (Newegg.com n.d. Newegg.).

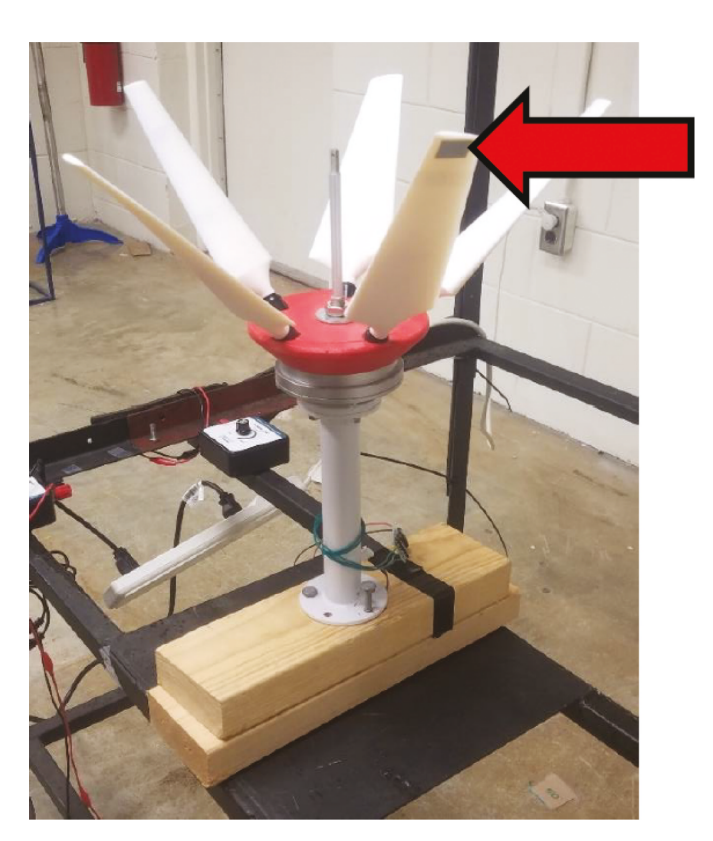


Figure 7. RPM measurement set-up denoting the placement of reflective tape.

A reactional torque meter is used to gage the torque as it relates to the increase of wind speed. For each wind speed, torque is recorded every 20 degrees of turbine rotation. The torque meter, depicted in Figure 8 is the Lutron TQ-8800, is calibrated using a dial torque wrench. It can monitor torque in 3 different units (Kg_f·cm, Lb_f·in and N-cm), and has a maximum of 147.1 N-cm with the accuracy of ±1.5%. The torque meter has a chuck clamp and only fits an 11/16 (0.5625)

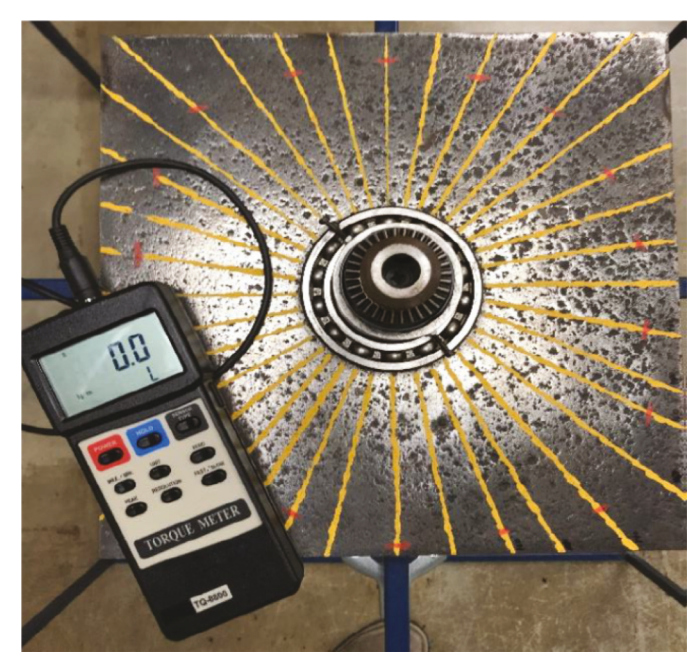


Figure 8. Lutron TQ-8800 torque meter configuration.

inch shaft, therefore a mechanism has to design to fit this chuck that is rigid enough to withstand the wind loads as well as the weight of each turbine model configuration while holding the assemblies in place so that an accurate torque reading can be acquired. It is important to note that all blades root sections, rotors hub sections, and torque measurement lock-up techniques are designed using ASME Y14.41-2009 standard for dimensioning and tolerance.

4. Numerical analysis

This section is divided into two parts, (i) static structural analysis and (ii) aerodynamic analysis. The structural section is further divided and discussed as static loading response, fatigue loading response as well as modal analysis. To study these structural and aerodynamic characteristics of the various rotors in this study, numerical simulations are performed using commercial Finite Element Analysis (FEA) and Computational Fluid Dynamics (CFD) software, ANSYS-FLUENT.

4.1. Static structural analysis

The equation given in The International Electro-Technical Commission's (IEC), IEC61400 2 (I. Commission, IEC 61400-2: Wind Turbines-Part 2), sums up the force from impending wind (Aerodynamic force) as follows:

$$F_a = C_f \frac{1}{2} \rho V^2 A_B \tag{1}$$

where, C_6 is the force coefficient, and can either be from lift or drag; and A_B is the component area that is appropriate for the force coefficient. For airfoil shapes, the area shall be the planform area (I. Commission, IEC 61400-2: Wind Turbines-Part 2).

The design wind pressure, p_Z represents the pressure exerted by the wind at any height, z and can be represented by the expression:

$$p_z = \frac{1}{2}\rho V^2 \tag{2}$$

The aerodynamic loads due to a parked rotor are depicted for each wind speed in Table 2. These pressure loads are implemented to assess the structural response of the blades.

The International Electro-Technical Commission (IEC), utilizes an equation for which they state estimates the wind gust an area may experience overtime based on its average wind speed. This is defined as the 50-year storm wind velocity:

Table 2. Wind speeds and corresponding pressure loads.

Tuble 2. Wind speeds and corresponding pressure loads.	
Wind Speed (m/s)	Pressure Load (Pa)
8 (design wind speed)	39.232
15	137.925
18	198.612
21	270.333
24	353.088
27	446.877
30	551.700
33	667.557
36	794.448

Table 3. Wind classification definition.

Parameters (m/s)	Class I	Class II	Class III	Class IV
Average wind speed	10	8.5	7.5	6
50 year return gust speed	70	59.5	52.5	42

$$V_{e50}(z) = 1.4V_{ref} \left(\frac{z}{z_{hub}}\right)^{0.11} \tag{3}$$

where, V_{ref} is the reference wind speed averaged over 10 min and Z_{hub} is the hub height.

In this work, it is assumed the expression $(z/z_{hub})^{0.11}$ is be equal to 1.0, since the turbine under study is not mounted at any height. Average wind speeds and the corresponding gust wind velocities can be seen in Table 3.

The data held in Table 4 portrays the forces calculated using equation (1). These forces are used to assess bending moments.

The total force acting on the turbine parts is the sum of aerodynamic force and centrifugal force:

$$F_t = F_a + F_c \tag{4}$$

Where

$$F_c = \frac{mV^2}{r} \tag{5}$$

Equation (5) is used to assess the force acting on the rotating turbine.

It is considered that due to the design of the blade and the fact that the size of these blades are small, there would not be significant gravitational forces from the blades weight to cause it to fail structurally. The same is assumed of edgewise loading. Therefore, the loading on the blade is only in the flapwise direction. Wind load mapping is done as a preliminary step in CFX just to assess how the wind is interacting with the blade, and to determine the most ideal way to represent each loading condition in the ANSYS Mechanical Modeler.

As stated earlier, the blades of this turbine are treated as cantilever beams. The loading case described in Figure 9 and Figure 10 denotes the load application for the static structural analysis.

Though it can be seen in Figure 9 that a pressure concentration at the tip of the blade the simulation is done as a load affecting the whole face of the turbine blade as depicted in Figure 10. This is deemed acceptable since this method of load application will effectively overestimate the effect of wind on the blade.

A medium unstructured mesh is developed for the span of blade, where, solid tetrahedral (SOLID187 and

Table 4. Wind speed with resulting forces.

Wind Speed (m/s)	B1 DESIGN (N)	B2 DESIGN (N)	B3 DESIGN (N)
8	114.65	94.12	44.49
15	403.07	330.88	156.42
18	580.43	476.47	225.24
21	790.03	648.53	306.58
24	1031.87	847.06	400.43
27	1305.96	1072.06	506.79
30	1612.30	1323.53	625.67
33	1950.88	1601.47	757.06
36	2321.71	1905.88	900.96

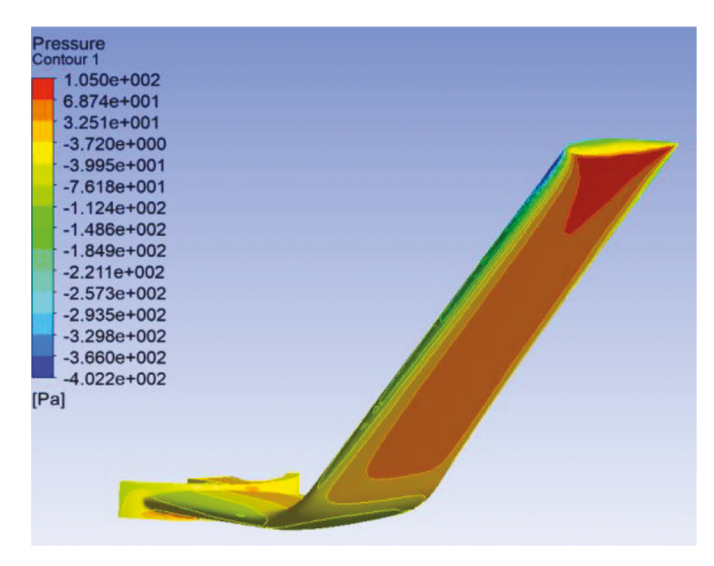


Figure 9. Wind load mapping.

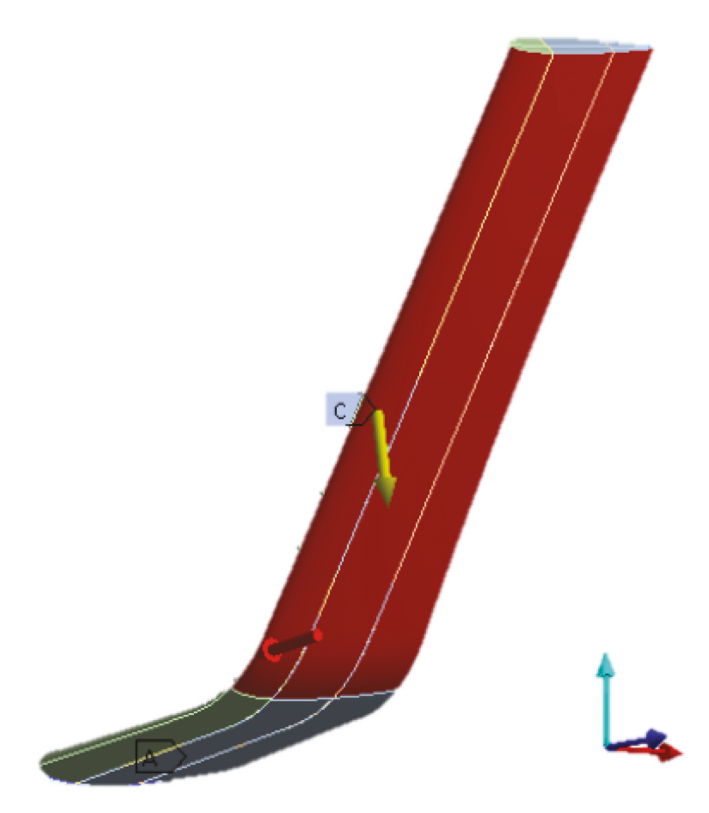


Figure 10. Analysis settings with flapwise loading.

SOLID186) elements are used. The root portions of blades design 1 and design 2 are meshed with solid hexahedral elements, and the thin features of the blade are meshed with SURF154. Blade 3 consisted of Hex20 and Wed15 elements.

4.2. Fatigue analysis

The fatigue analysis is done at 8 m/s wind speed. The rationale behind this decision is to assess the fatigue criteria under the design wind speed (8 m/s) in order to judge the longevity of the blade profiles. These conditions for this design would be considered normal operation.

The Goodman fatigue theory as expressed by equation (6) has been applied for the fatigue analysis part of this project. In general, most experimental data falls between the Goodman and Gerber theories with the Soderberg theory usually being overly conservative. The Goodman theory can be a good choice for brittle materials with the Gerber theory usually a good choice for ductile materials (Browell and Hancq 2006). The loading for this current analysis is fully reversed.

$$\frac{\sigma_{Alternating}}{S_{Endurance_Limit}} + \frac{\sigma_{Mean}}{S_{Ultimate_Strength}} = 1$$
 (6)

The loading for this project is set to zero-based since the simulation being targeted is the effect of centripetal force on the rotor blades as a cyclical load, in the same way it would occur as the turbine rotates to produce energy.

4.3. Modal analysis

Modal analysis interested only in the natural frequencies and the relative shapes of the vibration modes, the damping effect is usually neglected. Six Eigen modes are studied to analyze the most likely response that the turbine blades would have. The modes 1 to 6 are analyzed by fixing the section of the blade considered to be the root in each design and observing the total deflection in each frequency.

The mesh statistics for all three structural cases being analyzed and displayed in Table 5. The instances where many mesh elements are presented, represent the instances in which a fine mesh element is used. This is done to account for small details in each geometry or instance of analysis.

4.4. Static rotor aerodynamic analysis

ANSYS CFX solver is used to calculate the effects of wind flow in a steady state stationary flow field. The static conditions analyzed here are setup where the turbine is open to flow and laid out as demonstrated in Figure 11. The flow field is described in terms of the rotor's diameter. These dimensions allow for the flow to become fully developed and allow adequate spacing for reactions within the field to be displayed fully. One case of the mesh is displayed in Figure 12. Notice from the figure the inflation layers that are established to surround each blade for ANSYS to better estimate the behavior of fluid with the blade surface.

The inflation layers serve as a means of further discretizing the simulation field to infer the characteristics of wind interaction with the blades more accurately.

The summary of mesh statistics for the aerodynamic study is encapsulated in Table 6. Medium mesh settings are applied for all cases.

Boundary conditions for the simulations are taken from experimental data. These include air velocity and inlet speed and corresponding rotational speed of the blades. The pressure outlet is kept at constant atmospheric pressure. The blade walls are given a no slip condition (Salyers 2016).

Table 5. Summary of mesh statistics for structural study.

	Blade 1		Blade 2		Blade 3				
	Structural	Fatigue	Modal	Structural	Fatigue	Modal	Structural	Fatigue	Modal
Element	318610	371112	454710	216839	3258	3258	1296	1920	1920
Nodes	498880	747836	125699	364682	1480	1480	7716	9776	9776
Skewness	0.95	0.951	0.926	0.949	0.93	0.93	0.875	0.816	0.814
Element type	TET10, HEX20, WED15, PYR13	TET10, HEX20, WED15, PYR14	TET4, HEX8		TET10			HEX20	

4.5. Transient rotor aerodynamic analysis

The CAD models are imported into ANSYS Design Modeler, and fluid regions are added to the geometry. For transient three-dimensional analysis of VAWTs, two separate fluid domains are needed for simulation (Alaimo et al. 2015). A sphere 15 inches in diameter is enclosed around the model and is established as a rotating zone. A second zone which is stationary and represents the far field fluid flow domain is created with a rectangular box enclosure. The dimensions of the transient rotor analysis are established identical to the static. The entire three-dimensional computational domain is illustrated in Figure 13.

A sectional view of the mesh used in the transient dynamic flow study is included in Figure 14. This figure displays the mesh variation between the fluid zone and the rotating zone as well as the inflation layers around the blade profile. The inflation layers serve as a means of further discretizing the simulation field to infer the characteristics of wind interaction with the blades more accurately.

A mesh interface is created between the two zones. The interface is necessary because the nodes on the boundaries of the far field and rotational zones are intentionally nonconformal. The interface pairs these so that interpolation can occur, and fluid may pass into and out of the rotating region (Salvers 2016).

The summary of mesh statistics for the aerodynamic study is encapsulated in Table 7. Medium mesh settings are applied for all cases.

Boundary conditions for the simulations are taken from experimental data. These include air inlet speed and corresponding rotational speed of the blades. The pressure outlet is kept at constant atmospheric pressure. The blade walls are given a no slip condition and zero rotational velocity relative to the sliding mesh zone (equal to the rotating fluid domain) (Salyers 2016).

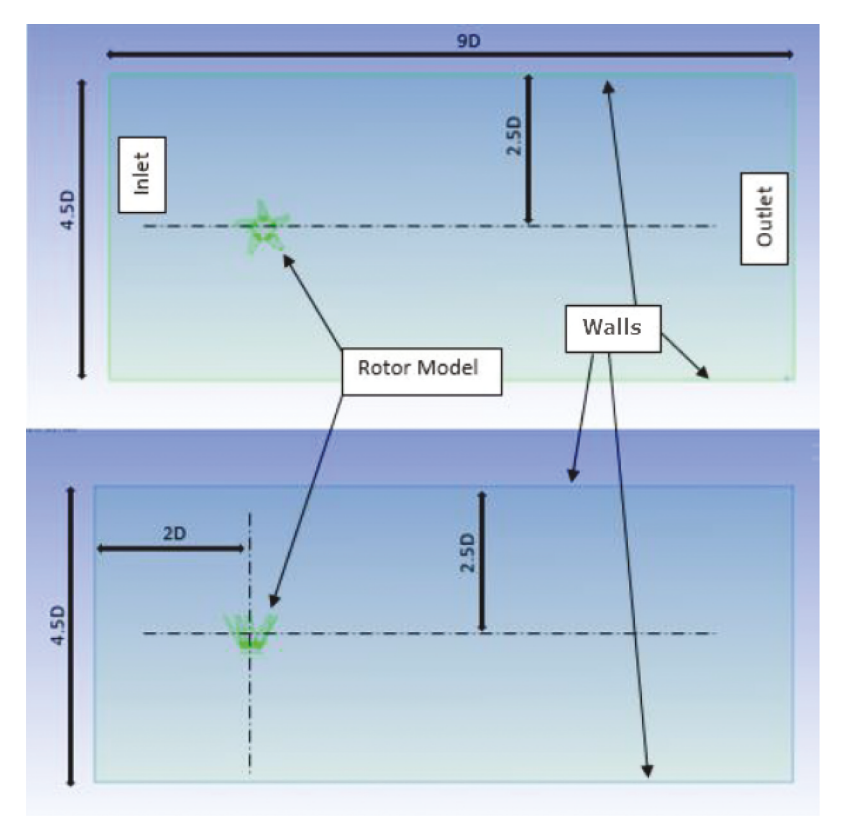


Figure 11. Three-dimensional computational domain for static conditions.

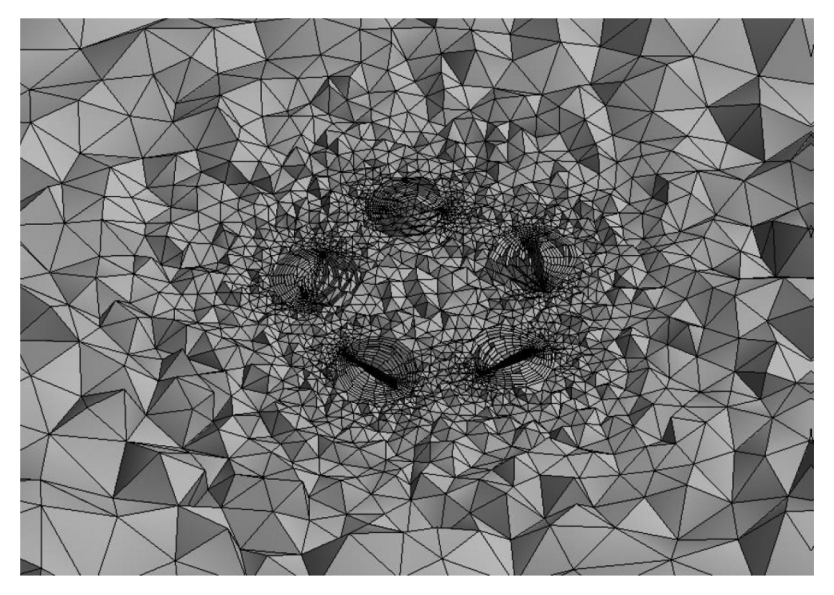


Figure 12. Static structural cut-away of mesh.

Table 6. Summary of mesh statistics for static aerodynamic study.

	3B45D	5B45D	5B45D (5deg)	5B60D
Element	323916	404200	479290	512087
Nodes	91345	167460	115939	184956
Skewness	0.93	0.95	0.922	0.961
Element type	TET4, WED6, PYR5	TET4, WED6, PYR5	TET4, WED6, PYR5	TET4, WED6, PYR5

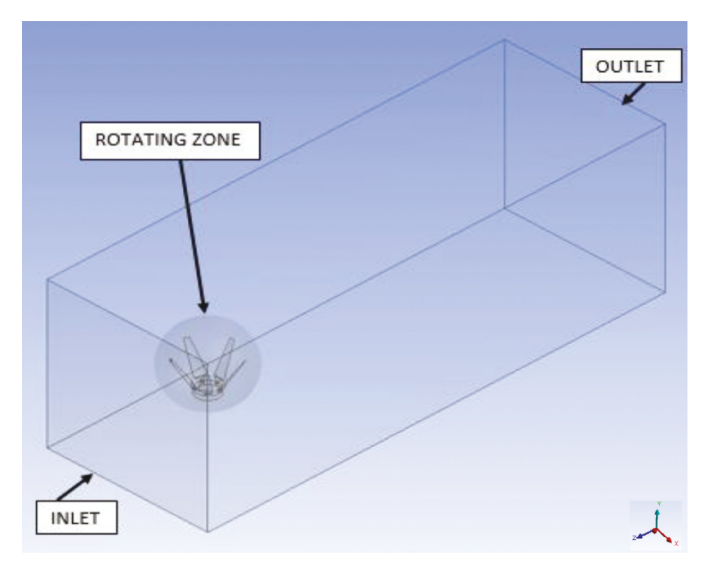


Figure 13. Three-dimensional domain of moving mesh.

4.6. Turbulence and flow model

Standard $k-\epsilon$ (SKE) model is the most widely-used engineering turbulence model for industrial applications. This model is robust and reasonably accurate and contains sub-models for compressibility, buoyancy, combustion, etc. However, of course it has limitations, such as, the ϵ equation contains a term which cannot be calculated at the wall. Therefore, wall functions must be used. Also, generally performs poorly for flows with strong separation, large streamline curvature, and large pressure gradient. Therefore, in both instances of the fluid flow analysis (static and dynamic) the k-epsilon (K- ϵ) model is

used along with a scalable wall function to determine the turbulence behavior within the fluid domain.

The incompressible flow is described by the Navier-Stokes equations 7 and 8. Equation 7 represents the continuity equation, while equation 8 is represents the momentum equation.

$$\frac{\partial u_j}{\partial x_i} = 0 \tag{7}$$

$$\frac{\partial u_j}{\partial t} + u_i \frac{\partial u_j}{\partial x_i} = -\frac{1}{\rho} \frac{\partial p}{\partial x_j} + v \frac{\partial^2 u_j}{\partial x_i^2}$$
 (8)

As mentioned earlier, generally the numerical computation of high-Reynolds number flows, employs the Reynolds decomposition given by equations 9 and 10.

$$u_i = \bar{u}_i + u_i' \tag{9}$$

$$p = \overline{p} + p' \tag{10}$$

For aerodynamic computations, of steady-state flow, the Reynolds-averaged Navier-Stokes (RANS) equations are usually employed. The RANS approach is a time-averaging of the Navier-Stokes equations. Thus, the time-averaging is given by equation 11.

$$\overline{u_i \frac{\partial u_j}{\partial x_i}} = \frac{\partial}{\partial x_i} \left(\overline{u_i u_j} \right) + \frac{\partial}{\partial x_i} \overline{\left(u_i' u_j' \right)} = \overline{u_i} \frac{\partial \overline{u_j}}{\partial x_i} + \frac{\partial}{\partial x_i} \overline{\left(u_i' u_j' \right)}$$
(11)

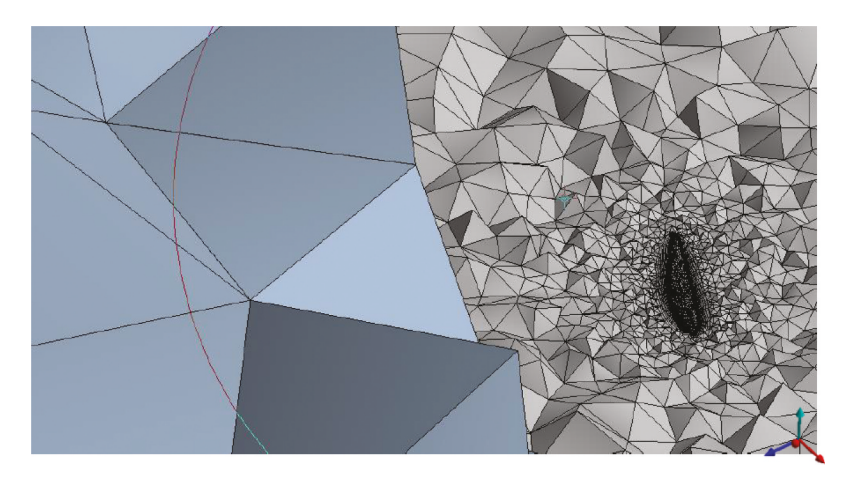


Figure 14. Section view of transient mesh.

Table 7. Summary of mesh statistics for transient aerodynamic study.

	3B45D		5B	5B45D		5B45D (5deg)		5B60D	
	Static Transient	Dynamic Transient	Static Transient	Dynamic Transient	Static Transient	Dynamic Transient	Static Transient	Dynamic Transient	
Element	323916	498135	404200	457340	479290	434197	512087	2629624	
Nodes	91345	724318	167460	172078	115939	293447	184956	498262	
Skewness	0.93	0.946	0.95	0.91	0.922	0.95	0.961	0.954	
Element	TET4, WED6,	TET4, WED6,							
type	PYR5	PYR5	PYR5	PYR5	PYR5	PYR5	PYR5	PYR5	

As seen from equation 11, there is a correlation between the fluctuating velocities due to the non-linearity of the convective term.

$$\frac{\partial \overline{u_j}}{\partial t} + \overline{u_i} \frac{\partial \overline{u_j}}{\partial x_i} = -\frac{1}{\rho} \frac{\partial \overline{p}}{\partial x_i} + \frac{\partial}{\partial x_i} \left(v \frac{\partial \overline{u_j}}{\partial x_i} - \overline{u_i' u_j'} \right)$$
(12)

i, j = 1, 2, 3

The term $-\rho u_i'u_i'$, represents the Reynolds stress tensor and is given by equation 13.

$$\tau_{ij} = -\rho \overline{u_i' u_j'} \tag{13}$$

i, j = 1, 2, 3

The turbulent stress tensor $\tau_{ij} = -\rho u_i' u_i'$ needs to be modeled. Most of the turbulence models employ an eddy viscosity model such as the one given in equation 14.

$$-\overline{u_{i}'u_{j}'} = v_{t} \left(\frac{\partial \overline{u_{i}}}{\partial x_{i}} + \frac{\partial \overline{u_{j}}}{\partial x_{i}} \right) - \frac{2}{3} \overline{k} \delta_{ij}$$
 (14)

In the present study, the $k - \omega$ turbulence model is used. Second-order numerical schemes are used for the space and time discretization.

4.7. Post processing

Simulations data are processed using Excel software. The equations (1) - (6) are used for structural calculations, and the equations (7) - (21) are be used to assess the aerodynamic performance. Once all simulations and experimental results are obtained the main parameters that will be known are reactional torque and transient torque, therefore, analysis must be done to compare the performance of the models to other research.

Nondimensional coefficients are used for comparison to other similar research and validation of the experiment. Three universally used nondimensional entities are considered for this study. The power coefficient describes the energy conversion efficiency of the turbine. Torque coefficient is a nondimensional representation of rotor torque, which is proportional to power produced. Tip-speed ratio is defined as the ratio of the blade tip speed to the free-stream wind velocity (MacPhee and Beyene 2012).

Rotor Swept Area

$$A_s = DH \tag{15}$$

Angular Velocity

$$\omega = \frac{2N}{60} \tag{16}$$

Tip speed Ratio

$$=\frac{\omega D}{2V}\tag{17}$$

Power

$$P = T\omega \tag{18}$$

Power Coefficient

$$C_p = \frac{P}{\frac{1}{2}\rho AV^3} = \frac{T\omega}{\frac{1}{2}\rho AV^3} = C_m$$
 (19)

Torque Coefficient

$$C_m = \frac{T}{\frac{1}{4}V^2} \tag{20}$$

Betz Limit Power

Table 8. Dimensions used in rotors basic parameters.

Rotor Name	Height (m)	Diameter (m)	Area (m²)
3B45D	0.1798	0.414	0.074
5B45D	0.1798	0.421	0.076
5B45D (5deg)	0.1798	0.421	0.076
5B60D	0.217	0.329	0.071
Average Area			0.0743

$$P_{Betz} = \frac{1}{2} \rho A_s C_{p_Betz} V^3 \tag{21}$$

In order to begin processing the data information about each turbines basic geometry are needed. The information detailed in Table 8 gives the basic parameters of each turbine rotor.

5. Results and discussion

5.1. Static structural results

Maximum Von-Mises Equivalent stress versus wind speed for the three blade designs are shown in Figure 15. The result shows that for blade 1 the maximum equivalent stress is from 1.26 MPa to 17.72 MPa, for blade 2 the maximum equivalent stress is from 1.49 MPa to 15.21 MPa and for blade 3 the maximum equivalent stress is from 2.27 MPa to 13.05 MPa which are all well below the specified material limit of 71.5MPa for ABS plastic. Blade 1 proved to have the highest maximum equivalent stresses at every wind speed of all three models.

Figure 16 depicts the displacement in each blade profiles versus wind speed. Blade 3's design showed consistently the largest displacement over the course of the wind rage with its minimum deflection that is about 2.82% (12.9 mm), and a maximum of 15.62% (71.4 mm) of the blades overall length. The other blade models being studied seemed to keep a more stable deflection ranging from 0.09% (0.42 mm) to 1.02% (4.66 mm) and 0.577% (2.64 mm) to 3.33% (15.21 mm) of the blade's overall length for designs 1 and design 2, respectively. Blade design 1 and design 2 are deemed acceptable since the deflection experienced by these designs are less than the 10% of overall blade length throughout the entire wind range criteria initially established. Blade design 3, however, violated this standard. Blades 1, 2 and 3 showed a minimum factor of safety (FOS) of 2.60, 6.07 and 3.63 at 36 m/s, respectively.

The effect of gravity is only assessed on blade design 1 and added about 2 to 10% to the overall Von-Mises stress and does not seem to have a significant effect on displacement.

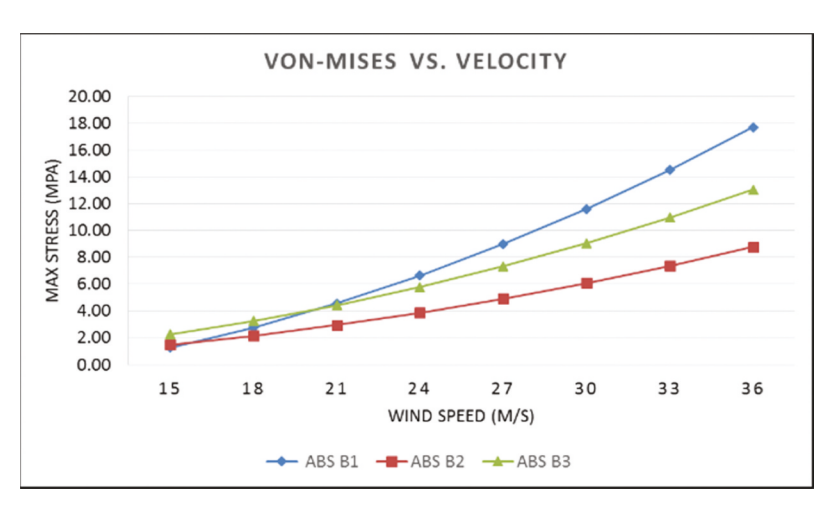


Figure 15. Flapwise maximum von-mises stress at various wind speeds.

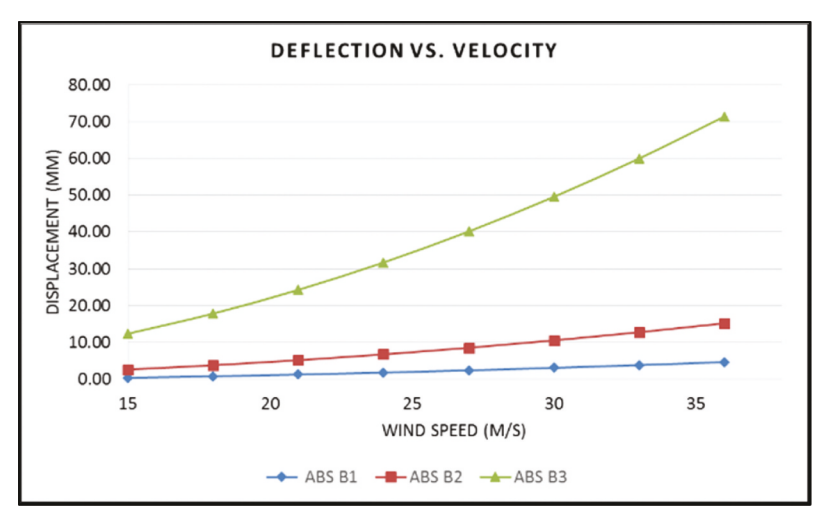


Figure 16. Flapwise displacement at various wind speeds.

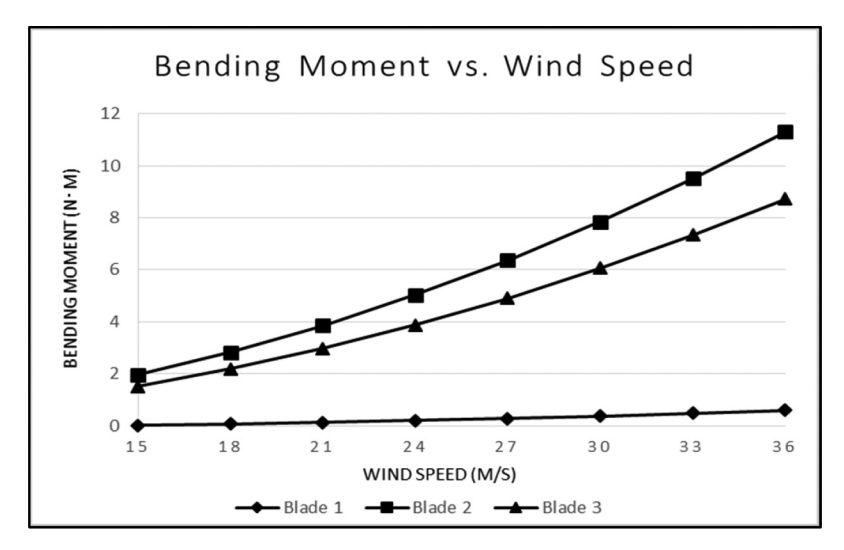


Figure 17. Bending moment at blade root at various wind speed.

Therefore, the effect of gravity is deemed negligible, and it is not included in the analysis of any of the other blades. This minimal effect of gravity is expected since the turbine size is small. There is a critical stress value appearing in the trailing edge of blade 1. This behavior is common in wind turbines with airfoil-shaped blades and can lead to catastrophic failures or at the very least a drastic reduction in aerodynamic efficiency (Marín et al. 2009).

In order to get a better understanding of how each blade is responding to the wind, the bending moment in each blade is assessed in terms of the same pressures used to load the blades for deflection and equivalent stress as illustrated in Figure 17. Note that the bending moment being assessed is at the root of each blade design, where they would relate to the hub. Taking the bending moment reactions at the root it is found that over the whole wind range, blade 2 suffered the highest bending moment of between 1.96 N.m - 11.31 N.m.

The centrifugal force from equation (5) plays an integral part in the longevity of a wind turbine blade, as the rotor turns this force is consistent at the root of the blade and is variable with wind speed as can be seen in Figure 18.

The highest centrifugal force observed is experienced by blade 1, and the lowest by blade design 3. This can be attributed to the fact that the design of blade 1 is more robust than the other two and has a greater mass.

5.2. Fatigue analysis results

The fatigue analysis (Table 9) revealed that mostly all the designs have more than enough longevity as can be seen from the life criteria reported in hours of life. This could be attributed to the fact that the loads are very small compared to the geometries and the material they are acting upon.

The results obtained from the fatigue analysis show that blade design 2 holds the highest stress response, at both the normal operating speed (8 m/s) outperforming blade 3 by 3.74% and what would be considered extreme case in terms of fatigue (15 m/s), outperforming blade design 3 in this instance by 79.89%. Therefore, blade design 2 could tolerate more stress before failing due to fatigue. From the three design cases, it can also be noted that blade design 2, in each case outperforms the other blades in average life by 45% in normal conditions and by 10% in the extreme condition. The study

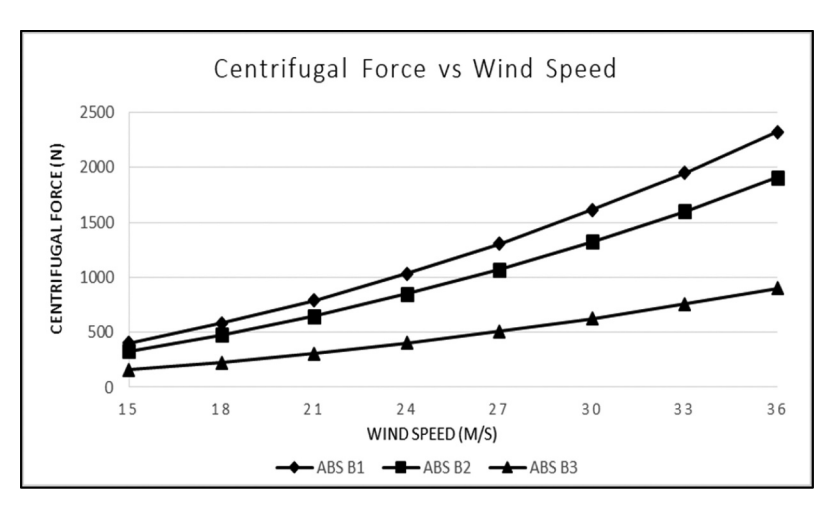


Figure 18. Centrifugal force through the wind range.

Table 9. Fatigue Analysis results.

	Fa	Fatigue @ 8 m/s			tigue @ 1	5 m/s
Blade Design	Equiv. V-M (MPa)	Min. FOS	Avg. Life (hrs)	Equiv. V-M (MPa)	Min. FOS	Avg. Life (hrs)
B1 B2 B3	- 19.59 18.87	0.044 2.56 2.66	0 1.45E+11 9.17E+10	- 14.82 6.36	0.0127 0.44 0.76	0 1.46E+10 1.32E+10

showed that there would be a catastrophic failure in blade design 1 within the first few iterations leading to safety values well below a factor of safety of 1 in both instances. Blade designs 2 and 3 both achieved a FOS value of greater than 1.5, as reported in Table 9. Equivalent stresses are not recorded for blade design 1 since the software reported that the design would fail.

Although this result reflects that there would be a failure region in the trailing edge of blade 1, this result could be due to the FEA software ANSYS having issues processing geometries with very small thickness.

5.3. Modal analysis results

The modal analysis is done as a final step in determining which blade would be chosen for optimization and move on to become the blade profile use in the test model for aerodynamic study. The first six blade modes in each design case are taken for analysis as these proved to be enough for the study. In each blade, the motion of the blade twisting or experiencing torsion about its planform area is the mode that give the most cause for concern. The frequency values of the blade modes that cause the largest displacement are 397.61 Hz (5th mode), 178.01 Hz (5th mode) and 123.37 Hz (4th mode), for blades 1, 2 and 3, respectively. Though these are not the highest frequencies in the range, they are quite large and the likely hood of any of the blades getting to these frequencies under normal operation is unlikely. The deformation experienced as a result of modal analysis are 446.82 mm, 207.74 mm and 203.25 mm for blade 1, 2 and 3, respectively.

Overall, Blade design 2 has the best results based on all the criteria set. The design showed an excellent Von-Mises stress response that is well below the yield strength of the material at 15.21MPa for static structural which achieves a FOS of 4.7 and 19.59MPa for fatigue which gives a FOS of 2.56 at normal design speed of 8 m/s. A maximum deflection at 36 m/s of 3.33% of the blades overall length (18 inches) is achieved. The Centrifugal force is also low throughout the wind range due to the lighter blade profile design. The design has the highest stress of all three designs during fatigue loading which tells us that it will endure a higher load before it succumbs to failure by fatigue stress.

5.4. Optimizing chosen blade

Blade design 2 optimized to reduce the effects of bending moment for experimental testing. The optimized blade profile can be seen in Figure 19. It is hypothesized that by adding a thicker blade root and moving the placement of the blade

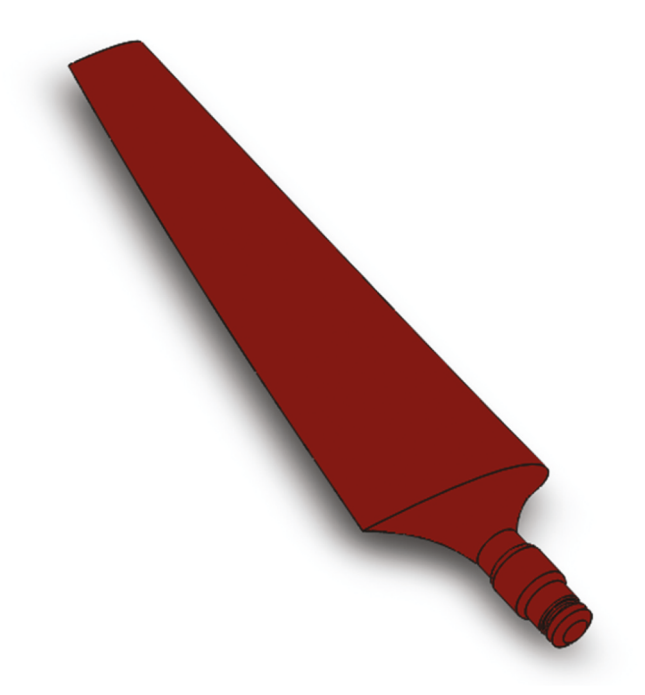


Figure 19. Optimized blade design.

root closer to the center of pressure of the airfoil shape there should be better response to bending stress.

5.5. Structural verification of chosen blade

The optimized design is tested at 15 m/s and using equation (4), a force of 1.26 N is obtained. The numerical tests showed that the resulting displacement in the blade is 0.278 mm (0.01 in) which is 0.1% of the overall blade length, equivalent stress of 0.802 MPa, a FOS of 15 and bending moment is 0.15 N.m for the static structural analysis.

The fatigue analysis of the blade yielded a safety factor of 15, an alternating equivalent stress of 0.401 MPa and a design life of 1.46E+11. The centrifugal force experienced in the design is 67.88 N, calculated from equation (5). This force is applied as a zero-based fatigue load in order to simulate the loading of the blade as it spins. The minimum life of the blade as a result is 1.76E+10 hours, FOS is 2.29 and Equivalent alternating stress is 21.86 MPa. A rotor model is then established from the blade profile (5-bladed with 45-degree inclination angle) and tested in the same way (Figure 20) to compare the results.

As can be seen in Figure 20, the aerodynamic resultant force is being assessed at 15 m/s where a conservative estimate of rotation is set at 500 RPM. The resulting fatigue response from this final structural verification of the turbine rotor is as follows: FOS is 1.87, Equivalent alternating stress is 16.91 MPa and a life of 1.02E+10 hours.

Notice from Table 10, the deformation of the rotor versus the single blade is 10.59% more, which can be attributed to the rotational velocity that is added. The stress, however, is 25.54% less in the rotor model than in the blade model. This difference is attributed to the way the rotor design is modeled in ANSYS in order to carry out structural analysis. There is also

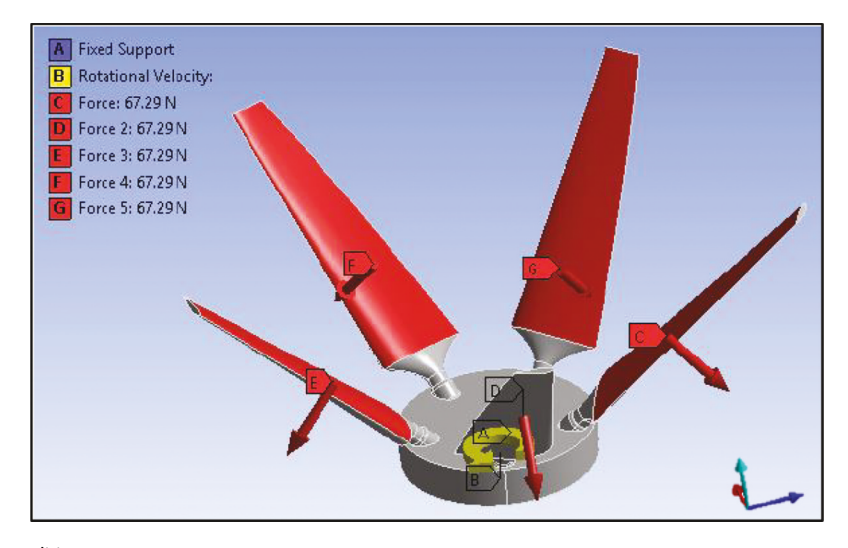


Figure 20. Structural boundary conditions on test rotor.

Table 10. Test model validation.

Component	Deformation (mm)	Equivalent Von-Mises (MPa)	Factor of Safety (FOS)
Rotor	16.69	16.91	1.87
Blade	15.01	21.86	2.29
Percent Diff. (%)	10.59	25.54	20.19

Table 11. Test rotors classification.

Rotor	# of Blades	Inclination Angle	Blade Pitch
3B45D	3	45	0
5B45D	5	45	0
3B60D	3	60	0
5B60D	5	60	0
3B45D	3	45	5
5B45D	5	45	5
3B60D	3	60	5
5B60D	5	60	5

a 20.19% percent difference in the factor of safety obtained for the single blade versus the rotor assembly.

As expected, the highest concentration of stress occurs in the regions where the blade is anchored in at the root, in both the rotor and blade model. One side of the models is experiencing tension as a result of loading and the reverse side is experiencing compression. The largest deformation occurs at the tips of the blade. Modal analysis is not performed on the rotor since it is assumed that the results of this analysis would give a similar result as those obtained for the three initial blade

designs. Also, and more importantly, it is already determined that the frequencies estimated by numerical study would not be seen by our models under real-world application. In the modal analysis the critical mode shapes would not be achieved at the low RPMs of this test design. The data discussed in this section is then use to fabricate eight rotor models. These rotor models will be further explored in the aerodynamic study.

Eight rotor models are developed as they are listed and described in Table 11. The rotor assemblies developed all applied the same airfoils shapes as depicted in Figure 21. NACA 0040 is used from the start of the aerodynamic section of the blade to 50% the length of the blade section, then NACA2414 is used on the remaining 50% of length. Once the rotor classifications are established, they are tested numerically to assess their performance. This initial test is done at the design speed of 8 m/s.

5.6. RPM measurement results

The transient analysis is done to obtain actual rotational speeds of each rotor. These values are necessary in order to establish the boundary conditions for the numerical study. The RPM measurements are taken as per the methods described previously. The gathered experimental data is translated to angular velocity and is represented in Figure 22. Note that the data depicted in Figure 22 is also used in the determination of the static aerodynamic study as well.

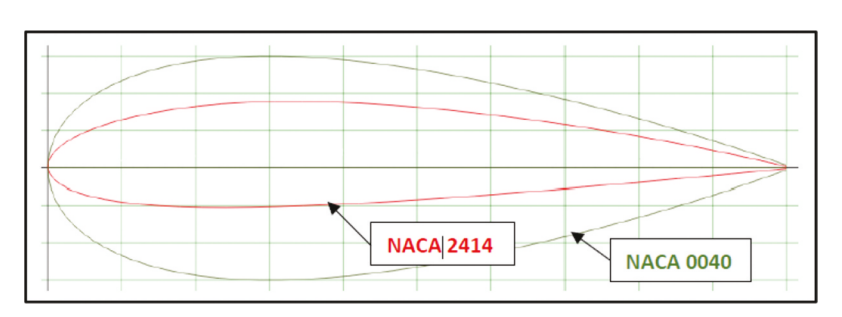


Figure 21. Airfoil description of all rotor models.

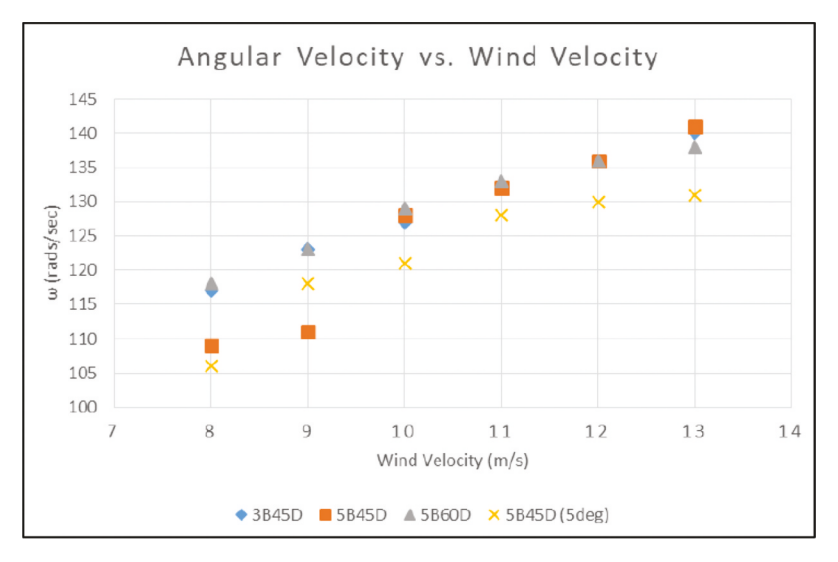


Figure 22. Experimental angular velocity vs wind velocity.

The summary of the collected data depicted in Figure 22 illustrates that 5B45D (5deg) turbine rotor has the lowest angular velocity at 8 m/s followed by the 5B45D rotor. The 3B45D and the 5B60D rotor model exhibited a superior angular velocity at the start of the wind range but is however matched by the 5B45D design from 10 m/s onwards. The 5B45D (5deg) maintained consistently the lowest angular velocity throughout the tested wind range except for at 9 m/s. It should be noted that there is no load on the turbine as it rotates. The results of this dynamic performance are from freely rotating rotors.

5.7. Aerodynamic analysis results

The numerical torque values obtained from ANSYS is displayed in Figure 23. This data gives us insight into which rotors are performing at a more optimal level, from the perspective of reactional torque. Reactional torque is used as the determining factor since this torque production gives a good indication of which turbine rotors have the best self- starting capabilities at 8 m/s. In order to better visualize the reactional toque, Figure 24 is created which displays the average values of each data set. This gives a good visual representation of where each turbine model stands.

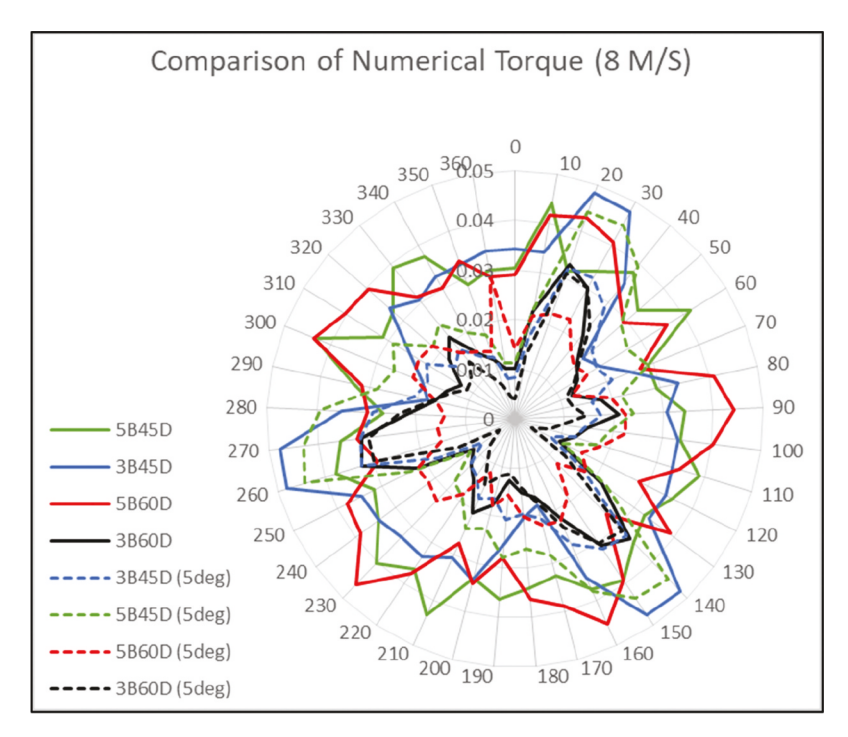


Figure 23. Comparison of established rotor torque at 8 m/s.

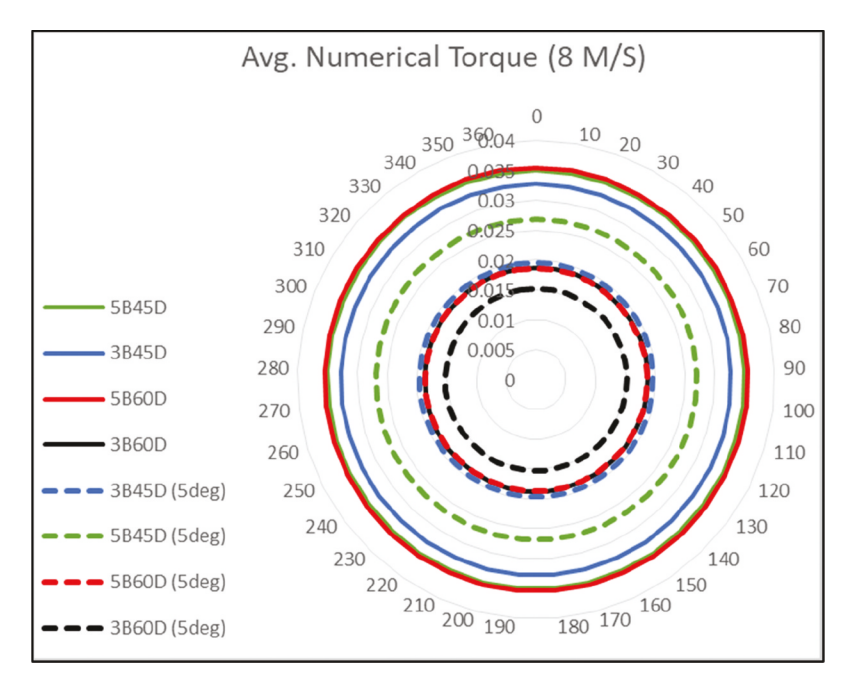


Figure 24. Comparison of established rotor average torque at 8 m/s.

From the average numerical reactional torque (Figure 24) it can be observed that at 8 m/s the 3B45D, 5B45D, 5B60D and 5B45D (5deg) rotor assemblies have the best self-starting potential. Applying equations (15) through (21), torque and power coefficients are calculated using these average reactional torque values in Figure 24. Average torque coefficient of 0.0591, 0.0554, 0.0599 and 0.0455 are presented for the 3B45D, 5B45D, 5B60D and 5B45D (5deg) rotor assemblies respectively, and power coefficient of 0.169, 0.159, 0.172 and 0.130, respectively, at these corresponding torque coefficient values.

In general, all five bladed rotors experience a spike in 5 regions of rotation, namely, between 10-30, 80-100, 140-170, 210-230 and 300-320 degrees. Each three bladed rotor experiences this same spike in 3 regions, namely, between 20-30, 140-150 and 260-270 degrees. After performing these initial tests as was stated earlier the most underwhelming rotor models are discarded from the study.

5.7.1. Static aerodynamic results

Displayed in Figure 25 is the numerical torque values as a function of azimuth angle for each turbine at 10 m/s and 12 m/s. The maximum torque value achieved at 10 m/s is around 0.076 N.m at 230 degrees by the 5B45D (5deg) rotor. This rotor is consistent in outperforming the other rotors through the entire wind range and achieves the highest torque value of 0.157 N.m at 300 degree. The performance of the other rotors is generally grouped together around a mean value.

The numerical torque coefficient versus azimuth angle for 8 m/s, 10 m/s and 12 m/s are illustrated in Figure 26. Once the torque coefficient (C_m) is calculated, it can be seen that 5B45D (5deg) has a wide spanning oscillation going from a low value

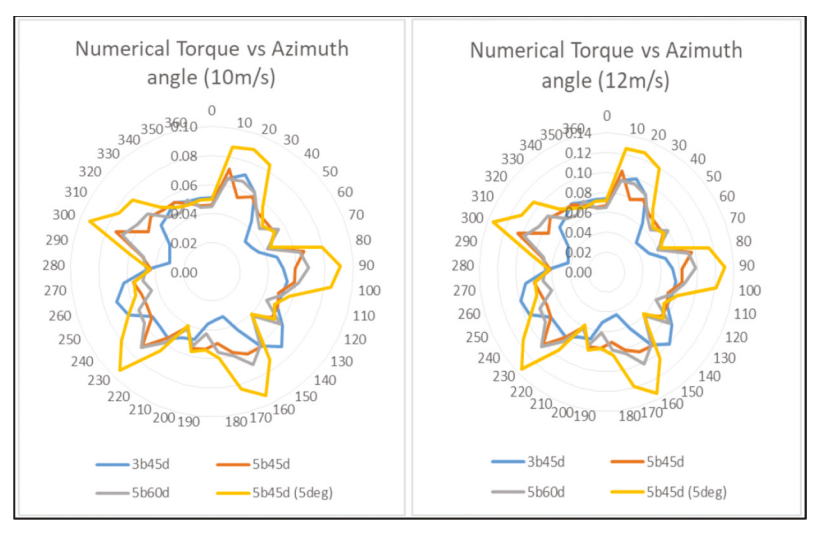
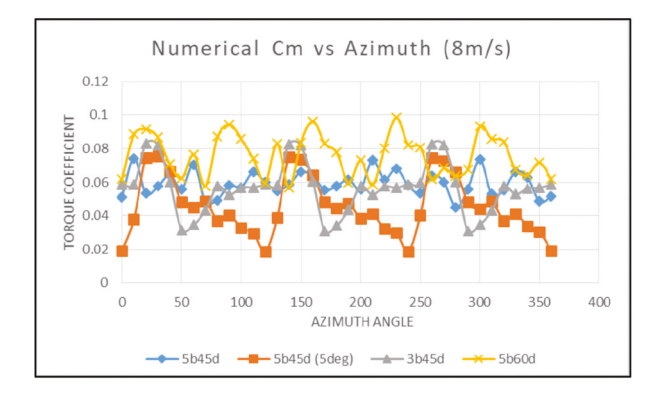
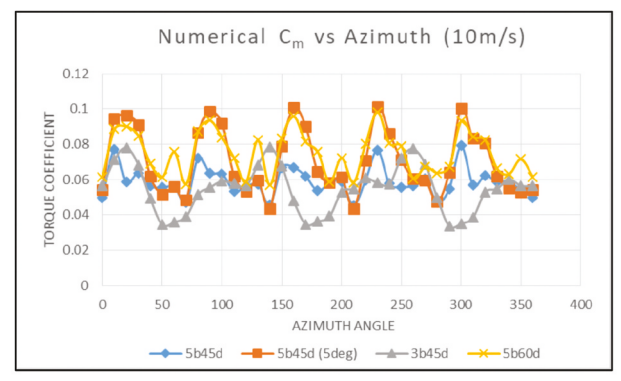


Figure 25. Numerical Torque vs. Azimuth angle at 10 m/s and at 12 m/s.





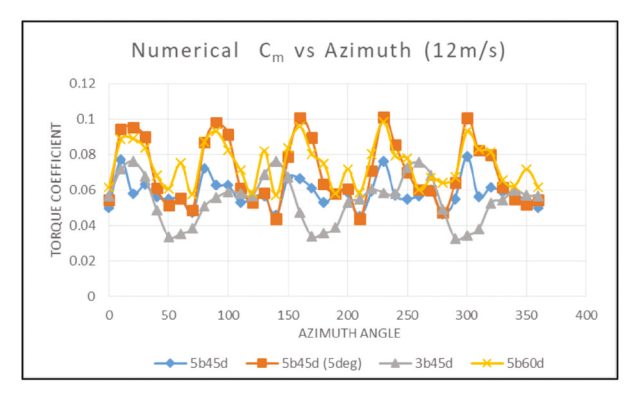


Figure 26. Numerical Torque coefficient vs. Azimuth angle at 8 m/s, 10 m/s and 12 m/s.

of 0.0185 at 120 degree to a high of 0.0754 at 30 degrees, these values corresponded to power coefficient (C_p) value of 0.052 and 0.21. For numerical torque coefficient, beginning at 9 m/s and up to 13 m/s the general shape and magnitude of the torque coefficient versus azimuth angle graphs remain the same for all rotors. This indicates that the torque response efficiency between these wind speeds generally remain constant among all the turbine models.

Figure 27 depicts the results of experimental torque at 8 m/s, 10 m/s, and 12 m/s. Unlike the numerical data, the experimental data do not have identifiable peaks and valleys. The peaks and valleys do not give a clear indication of the number of blades used in each rotor case. Also, unlike the numerical data the experimental data shows the 5B45D (5deg) to be the worst performing rotor assembly and instead the 5B45D rotor is the best performing rotor.

Data obtained from the experimental investigation is processed and mean and maximum values recorded for both numerical and experimental analysis. Using equations (15)

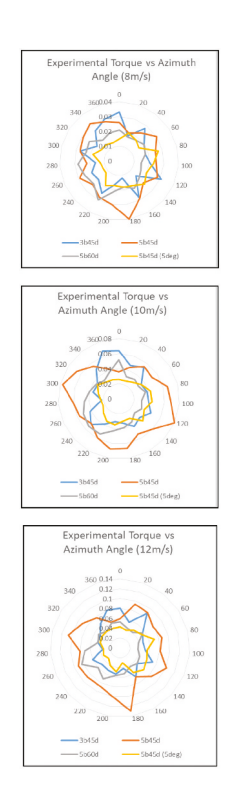


Figure 27. Experimental Torque vs. Azimuth angle at 8 m/s, 10 m/s and 12 m/s.

Table 12. Static aerodynamic results summary.

Numerical					
Rotor	Diameter (m)	V (m/s)	TSR	C _m	C _p
3B45D	0.414	8	3.0274	0.08291	0.25099
		10	2.6289	0.07826	0.20575
		12	2.3460	0.07634	0.17910
5B45D	0.421	8	2.8681	0.07430	0.21309
		10	2.6944	0.07918	0.21333
		12	2.3857	0.07885	0.18811
5B45D (5deg)	0.421	8	2.7891	0.07536	0.21018
		10	2.5471	0.10133	0.25809
		12	2.2980	0.10109	0.23052
5B60D	0.329	8	2.4264	0.09847	0.23894
		10	2.1221	0.09839	0.20879
		12	1.8918	0.09832	0.18331
Experimental					
Rotor	Diameter (m)	V (m/s)	TSR	C_{m}	C_p
EX-3B45D	0.414	8	3.0274	0.05672	0.17170
		10	2.6289	0.07370	0.19374
		12	2.3460	0.06798	0.15949
EX-5B45D	0.421	8	2.8681	0.06760	0.19389
		10	2.6944	0.08653	0.23315
		12	2.3857	0.13000	0.23296
EX-5B45D (5deg)	0.421	8	2.78913	0.04563	0.12727
		10	2.54705	0.04759	0.12122
		12	2.29796	0.07100	0.12162
EX-5B60D	0.329	8	2.42638	0.06399	0.15527
		10	2.12205	0.07372	0.15643
		12	1.89175	0.08400	0.14846

through (21), the derived torque values are used to calculate torque coefficient ($C_{\rm m}$) and power coefficient ($C_{\rm p}$) as shown in Table 12. This table shows the comparison of the different rotor assemblies in terms of their diameter, operating TSR, maximum recorded torque coefficient ($C_{\rm m}$) and power coefficient ($C_{\rm p}$) at wind speed of 8 m/s, 10 m/s, and 12 m/s.

Numerically derived torque coefficients from each turbine is illustrated in Figure 28. The numerical torque coefficient (C_m)

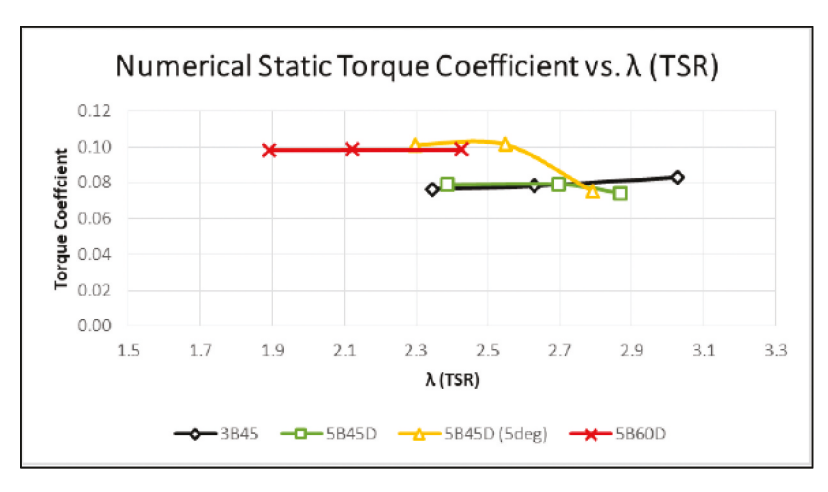


Figure 28. Numerical Torque Coefficient vs. TSR.

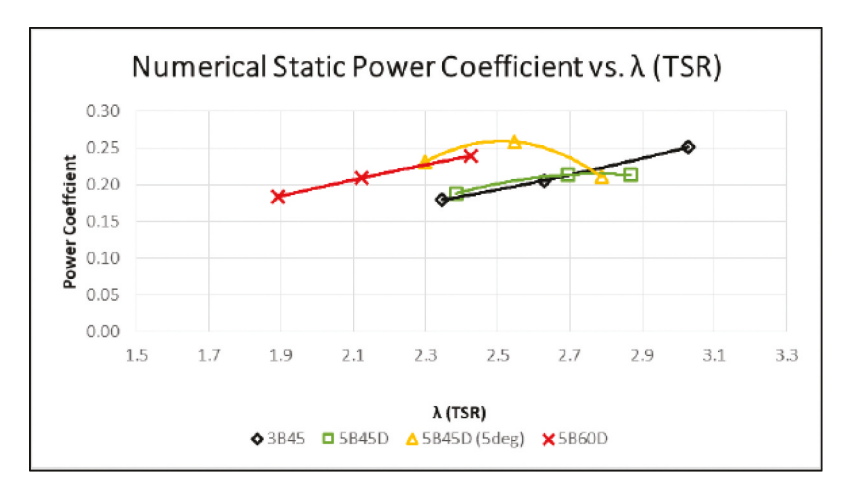


Figure 29. Numerical Power Coefficient vs. TSR.

variation with the change of Tip Speed Ratio (TSR) for each turbine is displayed in the figure. It can be seen that 5 bladed rotor with a 45 degree angle of inclination and 5 degree of blade twist at a TSR of 2.54 has achieved the highest torque coefficient.

Figure 29 depicts the numerical power coefficient (C_p) as a function of the TSR. It should be noted that at a TSR of 2.54 the highest power coefficient of 0.258 is achieved by the 5B45D (5deg) turbine rotor. Observe that the 5 bladed 60-degree rotor produces its power at a lower tip speed ratio (TSR) than the

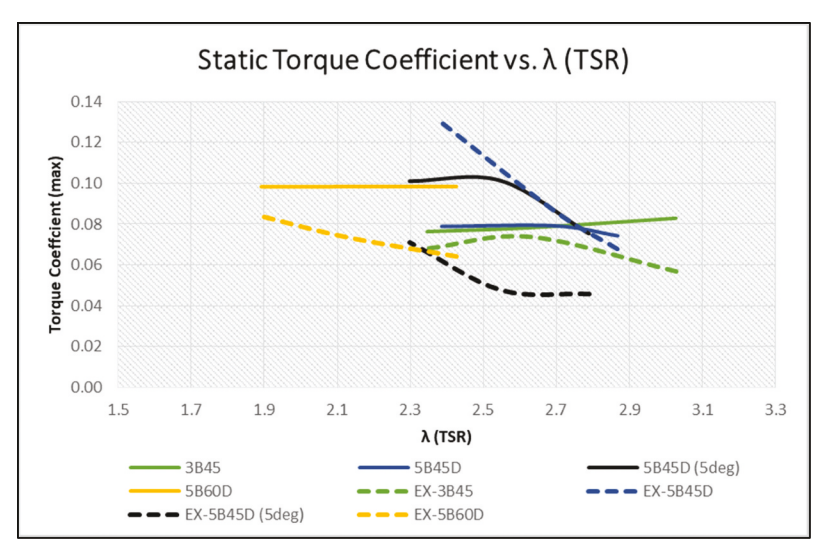


Figure 30. Torque Coefficient vs. TSR.

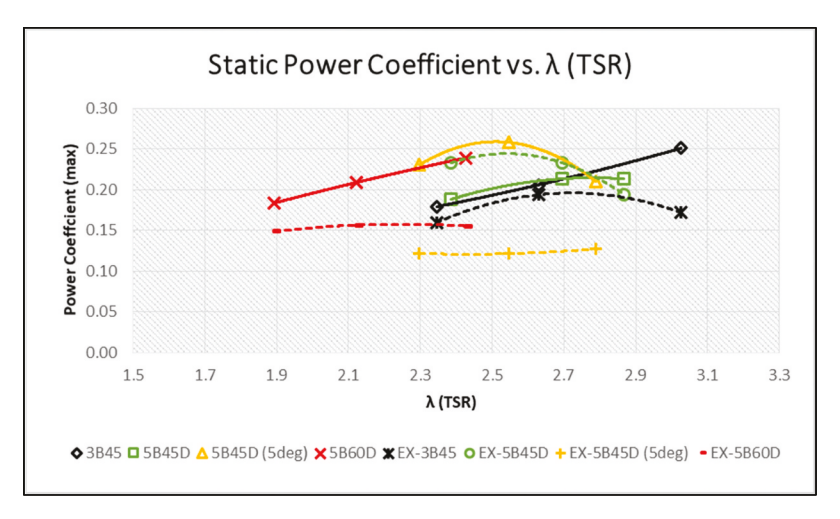


Figure 31. Power Coefficient vs. TSR.

other rotor assemblies. The 3 bladed 45-degree rotor produces the second highest power coefficient of 0.251 at a TSR of 3.03. The 3B45D rotor also produces the lowest Cp of 0.18 at TSR 2.35 and overall the 3B45D operates over the largest range of TSR.

Figure 30 and Figure 31 display the combination of numerical results alongside the experimental results. The experimental results are labeled with the prefix 'EX' for clarity. The data for the 3 bladed 45-degree rotor assembly is the only data that appeared to be coherent for both numerical and experimental data. There is a maximum percent difference of 37.51%.

It can be observed from Figure 30 and Figure 31 that both numerical and experimental results have relatively good agreement except the 5B45 (5deg) rotor assembly which exhibits a very dramatic incoherence with the experimental and numerical results. It is noted that the 5B60D rotor preferred a lower

Table 13. Transient results summary.

Experimental				
Rotor	TSR	Wind Speed (m/s)	C_p	C _m
EX-3B45D	3.027375	8	0.039876	0.013172
	2.6289	10	0.096781	0.036814
	2.346	12	0.123038	0.052446
EX-5B45D	2.868063	8	0.042015	0.014649
	2.6944	10	0.096204	0.035705
	2.385667	12	0.155942	0.065366
EX-5B45D (5deg)	2.789125	8	0.007351	0.002636
	2.54705	10	0.032382	0.012713
	2.297958	12	0.044139	0.019208
EX-5B60D	2.426375	8	0.027429	0.011305
	2.12205	10	0.065524	0.030878
	1.89175	12	0.071099	0.037584
Numerical				
Rotor	TSR	Wind Speed (m/s)	C_p	C_{m}
3B45D	3.027375	8	0.067535	0.022308
	2.6289	10	0.097997	0.037277
	2.346	12	0.057702	0.024596
5B45D	2.868063	8	0.259812	0.090588
	2.6944	10	0.187366	0.069539
	2.385667	12	0.129399	0.05424
5B45D (5deg)	2.789125	8	0.019051	0.006831
	2.54705	10	0.015716	0.00617
	2.297958	12	0.021047	0.009159
5B60D	2.426375	8	0.099177	0.040315
	2.12205	10	0.088115	0.040955
	1.89175	12	0.075442	0.039912

operating TSR than the other rotor models for both experimental and numerical cases.

It should be noted that all numerical results are being assessed after about 5 seconds of rotation and all experimental results are assessed after 120 seconds of rotation. The values represented are only done for wind speeds of 8 m/s, 10 m/s and 12 m/s and are plotted the maximum values of the torque and power coefficients.

5.7.2. Transient aerodynamic results

Table 13 depicts a summary of transient dynamic results for both experimental and numerical study. These results are at 8 m/s, 10 m/s and 12 m/s wind speeds.

The maximum transient value of power coefficient (C_p) obtained is 0.259 as shown in Table 13 achieved by the 5 bladed 45-degree rotor numerically at a TSR of 2.87. Whereas the experimental power coefficient (C_p) value at the same TSR is 0.042, which shows a very large percent difference. Figure 32 graphically summarizes the results expressed in Table 13.

Transient numerical versus transient experimental power coefficient as a function of TSR is displayed in Figure 32. As can be identified from the figures, the results coincide, however, there are instances where the experimental set-up is performing better than the numerical model. There are also large discrepancies in the results, especially with the 5B45D rotor model. This would suggest that either the numerical setup is too conservative, or the experimental setup has inconsistencies.

It should be noted that throughout this work, the 3B45D rotor has given excellent agreement in both experimental and numerical testing. The difference in the obtained efficiencies can be attributed to the transient study being conducted under load versus values collected in the static portion of the study, which are theoretically calculated from obtained torque measurements.

6. Conclusions

From this current research the following conclusions can be made:

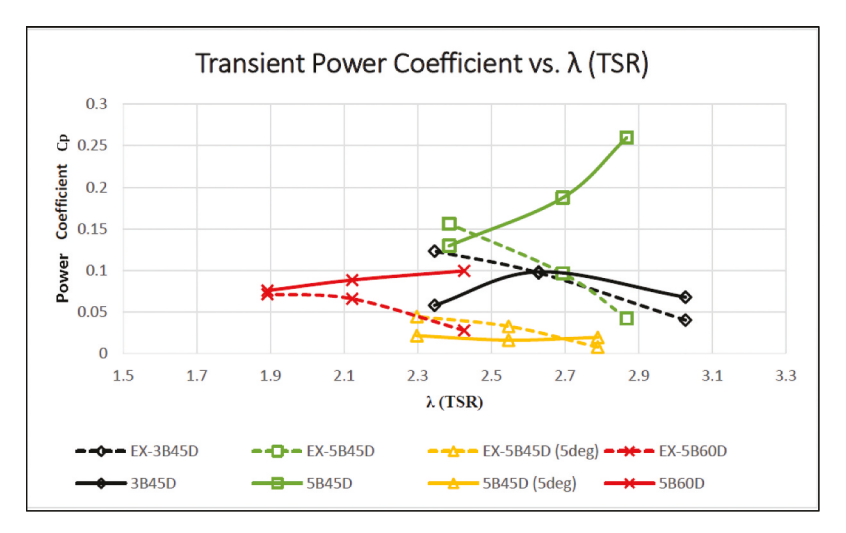


Figure 32. Transient Power Coefficient vs. TSR.

In accordance with IEC wind turbine design codes, the chosen blade geometry and subsequent rotor assembly are structurally safe enough to run physical tests. The blade geometry of blade design 2 out did all other models in every criterion. Therefore, it was chosen for aerodynamic study. The redesigned rotor design has a fatigue loading FOS of 1.87 for a wind speed of 8 m/s and a resulting life of 1.02E+10 hours. While the blade showed a life of 1.76E+10 hours and a FOS is 2.29. This corresponded to a difference of \sim 20% in FOS. The achieved FOS was higher the set criteria of FOS greater than or equal to 1.5.

Highest average power coefficient observed in the static aerodynamic study is 0.258 which is obtained numerically by the 5B45D (5deg) rotor at a TSR of 2.54. The rotors operate between a TSR of 1.8 and 3.03, with the 5B60D rotor performing at a lower TSR than the other rotors which had a 45-degree incline. The 3B45D rotor produces the second highest power coefficient of 0.251 at a TSR of 3.03 and this rotor assembly gives the best agreement with both numerical and experimental results. In terms of consistency in the results, the 3B45D rotor performed the most consistent with power coefficient values. Power coefficient from static aerodynamic simulation is 0.206, whereas static experimental power coefficient is 0.194 both at TSR = 2.63 which is ~6% difference. Also, the 3B45D rotor assembly covered the widest range of TSR.

The maximum transient value of power coefficient (C_p) obtained is 0.259 achieved by the 5B45D rotor numerically at a TSR of 2.87, whereas the experimental power coefficient (C_p) value at the same TSR is 0.042, which shows a very large percent difference.

It should be noted that throughout this work, the 3B45D rotor has given excellent agreement in both experimental and numerical performance.

The numerical conclusions achieved by this study are validated and accepted, while the experimental values obtained require more careful study to be reliable. Experimental methods need to be assessed and improved. The experimental studies would require better flow sampling at the inlet, as well eliminating any wall effects, such as increasing the size of the test section. Better data

acquisition for better accountability of the blade deformation.

Acknowledgments

Authors would express the heartiest deep sense of gratitude to Mechanical Engineering Department of Georgia Southern University. Authors acknowledge REU Site: Propulsion, Aerodynamics, Materials and Controls of Aerial Vehicles, Award #1950207.

References

Alaimo, A., A. Esposito, A. Messineo, C. Orlando, and D. Tumino. 2015. 3D CFD analysis of a vertical axis wind turbine. *Energies* 8 (4):3013–33. doi:10.3390/en8043013.

Barnes, R. H., E. V. Morozov, and K. Shankar. 2015. Improved methodology for design of low wind speed specific wind turbine blades. *Composite Structures* 119:677–84. doi:10.1016/j.compstruct.2014.09.034.

Belloli, M., I. Bayati, A. Facchinetti, A. Fontanella, H. Giberti, F. La Mura, F. Taruffi, and A. Zasso. August 15 2020. A hybrid methodology for wind tunnel testing of floating offshore wind turbines. *Ocean Engineering* 210: 107592. doi:10.1016/j.oceaneng.2020.107592.

Bir, G., and P. Migliore. 2004. "Preliminary structural design of composite blades for two and three-blade rotors," *Technical Report, NREL/TP-50031486*, September.

Browell, R., and A. Hancq. 2006. "Calculating and Displaying Fatigue Results," ANSYS Support. March 29.

Commission, I. 2006. IEC 61400-2: Wind turbines-part 2: Design requirements for small wind turbines. ed. Geneva, Switzerland: IEC.

Gardiner, G. 2011. HAWTs vs. VAWTs. *Composites Technology* 17 (4):30. Hand, B., and A. Cashman. 2017. Conceptual design of a large-scale floating offshore vertical axis wind turbine. *Energy Procedia* 142 (December):83–88. doi:10.1016/j.egypro.2017.12.014.

Hand, B., and A. Cashman. 2020. A review on the historical development of the lift-type vertical axis wind turbine: From onshore to offshore floating application. Sustainable Energy Technologies and Assessments 38 (April):100646. doi:10.1016/j.seta.2020.100646.

Kong, C., T. Kim, D. Han, and Y. Sugiyama. 2006. "Investigation of fatigue life for a medium scale composite wind turbine blade. The Third Int. Conf. On Fat. Of Comp 28 (10):1382–88.

Lei, H., J. Su, Y. Bao, Y. Chen, Z. Han, and D. Zhou. 2019 January 1. Investigation of wake characteristics for the offshore floating vertical axis wind turbines in pitch and surge motions of platforms. *Energy* 166:471–89. doi: 10.1016/j.energy.2018.10.101.



- Liu, X., L. Wang, and X. Tang. 2013. Optimized linearization of chord and twist angle profiles for fixed-pitch fixed-speed wind turbine blades. Renewable Energy 57:111-19.
- MacPhee, D., and A. Beyene. 2012. Recent advances in rotor design of vertical axis wind turbines. Wind Engineering 36 (6):647-66. doi:10.1260/0309-524X.36.6.647.
- Marín, J. C., A. Barroso, F. París, and J. Cañas. March 2009. Study of fatigue damage in wind turbine blades. Engineering Failure Analysis 16 (2):656-68. doi: 10.1016/j.engfailanal.2008.02.005.
- Newegg.com. n.d. Newegg. https://www.newegg.com/Product/Product. aspx?Item=152-000N-00046.
- Ronold, K. O., and C. J. Cristensen. 2001. Optimization of a design code for wind-turbine rotor blades in fatigue. Engineering Structures 23 (8):993-1004. doi:10.1016/S0141-0296(00)00109-7.
- Salyers, T. E. 2016. "Experimental and numerical investigation of aerodynamic performance for vertical-axis wind turbine models with various blade designs," Master's Thesis, Department of Mechanical Engineering, Georgia Southern University, Statsboro.
- Su, J., Y. Chen, Z. Han, D. Zhoua, Y. Bao, and Y. Zhao. 2020 February 15. Investigation of V-shaped blade for the performance improvement of

- vertical axis wind turbines. Applied Energy 260:114326. doi: 10.1016/j. apenergy.2019.114326.
- Toft, H. S., and J. D. Sorensen. 2011. Reliability based design of wind turbine blades. Structural Safety 33 (6):333-42. doi:10.1016/j. strusafe.2011.05.003.
- Wang, L. 2015. "Nonlinear aeroelastic modelling of large wind turbine composite blades," PhD Thesis, Coventry University, Coventry, West Midlands, United Kingdom.
- Wang, L., X. Tang, and X. Liu. 2012a. Blade design optimisation for fixedpitch fixed-speed wind turbines'. ISRN Renewable Energy 2012:1. doi:10.5402/2012/682859.
- Wang, L., X. Tang, and X. Liu. 2012b. "Optimized chord and twist angle distributions of wind turbine blade considering Reynolds number effects," International conference on wind energy: Materials, engineering and policies (WEMEP-2012), Hyderabad (India), 2223 November.
- Wang, L., A. Kolios, T. Nishino, P.-L. Delafin, and T. Bird. 2016. Structural optimisation of vertical-axis wind turbine composite blades based on finite element analysis and genetic algorithm. Composite Structures 153:123-38. doi:10.1016/j.compstruct.2016.06.003.
- Xfoil. n.d. Xfoil Prediction Polar: NACA 4 Digit Airfoil Generator.